A Temperature Gradient-Based Potential Defects Identification Method for IGBT Module

Bing Gao, Fan Yang, *Member, IEEE*, Minyou Chen, *Senior Member, IEEE*, Li Ran, *Senior Member, IEEE*,
Irfan Ullah, Shengyou Xu, and Philip Mawby, *Senior Member, IEEE*

***Abstract*—The paper presents a temperature gradient-based method for device state evaluation, taking the insulated-gated bipolar transistor (IGBT) modules as an example investigation. First, theoretical basis of this method is presented and the results from example calculation on temperature gradient indicate that the increased thermal resistance and power loss of IGBT modules would increase the temperature gradient. Then, an electrical–thermal–mechanical finite-element method model of IGBT modules, which takes the material temperature-dependent characteristic into account, is utilized to estimate the temperature gradient distribution for both healthy and fatigue conditions. It is found that the temperature gradient varies with power loss. Furthermore, both the experimental and simulation investigation on the temperature gradient for different conditions were conducted, and it is concluded that the temperature gradient can not only track the change of power loss, but also have a better sensitivity compared with temperature distribution. In addition, the temperature gradient can reflect the defects location and distinguish failures degree. In the end, the influence on the temperature gradient distribution caused by solder fatigue, void, and delamination is discussed.**

***Index Terms*—Defects identification, electro-thermal-mechanical, power module, solder fatigue, temperature gradient.**

I. INTRODUCTION

THE temperature behaviors of electrical equipment are of great interest for determining equipment state, especially the internal defects. When internal defects arise in electrical equipment, a rise of inside and surface temperature will happen; therefore, temperature measurement technology is widely used in condition evaluation of electrical equipment, including power transformers [1], circuit breakers [2], and power electronics [3], [4]. As one of the key components in power electronics systems, insulated-gated bipolar transistor (IGBT) modules are exposed to wear-out failures, including bond wire lift off and solder fatigue [5]. It is believed that the failure propagation will change the electrical and thermal behaviors of IGBTs. Information regarding its temperatures is important to ensure a reliable design of converter [6], [7].

Consequently, many researches are concentrated on the calculation, measurement, and application of thermal behavior in power modules condition evaluation, reliability design [8]–[10]. Selection of the approach to reliability design and condition monitoring for electronic products has been an evolutionary process [9]. At present, nondestructive testing techniques are reported in use such as scanning acoustic tomography [11] and active thermography [12]. Some thermal or electrical parameters are also adopted to monitor the degradation of power modules, and this method mainly concentrates on the surface response [13], or the transient electric parameters which are internal-failure-sensitive parameters [14]–[18]. Xiang *et al.* [13] proposed a method to monitor the solder fatigue by using the case-above-ambient temperature rise and developed a model to estimate thermal resistance ΔR_{th}. Xiang *et al.* [14] presented a method to evaluate solder fatigue in a voltage-source inverter IGBT module by detecting its output harmonic, of which the low-order harmonics are affected by the junction temperature. Zhou *et al.* [15] presented a method to monitor the internal crack of aluminum based on stray parameters identification, in which the least square method was employed to detect the stray parameters in IGBT. In [16], defects in IGBT module can be identified through dynamic change of the gate current, through which the influences on the parasitic elements caused by local aging damage can be distinguished. Bryant *et al.* [17] outlined a method to evaluate the internal condition by using the collector turn-off voltage $\mathrm{d}V/\mathrm{d}t$, and implication of temperature was also discussed. Patil *et al.* [18] presented a method to monitor the condition of IGBT by detecting the change of collector–emitter saturation voltage, and a prognostic system was developed. Most of these methods mainly rely on the sensitive of temperature or electrical parameters. It is known that the temperature field distribution of an equipment is a scalar field, and a vector corresponding to its gradient can be obtained to offer more information to this scalar field according to the basis of vector analysis. As a result, the vector field should be related to the device state.

On the basis of the previous work, a temperature gradient-based method is presented in the paper. Example calculation of IGBT is conducted, and then the method is validated against analytical analysis, finite-element method (FEM) simulation and

Manuscript received March 21, 2014; revised August 14, 2014; accepted April 13, 2016. Date of publication May 10, 2016; date of current version December 9, 2016. This work was supported by the National Natural Science Foundation of China under Grant 51477019, the National Basic Research Program of China under Grant 2012CB215205, and National Nature Science Foundation Key Project under Grant 51137006. Recommended for publication by Associate Editor H. Wang.

B. Gao, F. Yang, M. Chen, I. Ullah, and S. Xu are with the State Key Laboratory of Power Transmission Equipment & System Security and New Technology, School of Electrical Engineering, Chongqing University, Chongqing 400044, China (e-mail: gaobing.cqu@gmail.com; yangfancqu@gmail.com; mchencqu@126.com; irfan.ee@suit.edu.pk; sheng_you_xu@163.com).

L. Ran is with the State Key Laboratory of Power Transmission Equipment & System Security and New Technology, School of Electrical Engineering, Chongqing University, Chongqing 400044, China, and also with the School of Engineering, University of Warwick, Coventry CV4 7AL, U.K. (e-mail: l.ran@warwick.ac.uk).

P. Mawby is with the School of Engineering, University of Warwick, Coventry CV4 7AL, U.K. (e-mail: p.a.mawby@warwick.ac.uk).

Color versions of one or more of the figures in this paper are available online at http://ieeexplore.ieee.org.

Digital Object Identifier 10.1109/TPEL.2016.2565701

experimental results. The temperature gradient under different types of failure is investigated, including solder fatigue, voids, and delamination. Results indicate that temperature gradient has a better sensitivity compared with temperature and it can reflect the defects location.

The remaining parts are arranged as follows: The basis of the method is described in Section II, and the temperature gradient of IGBT module under steady and transient state is investigated in Section III. Section IV studies the characteristic of temperature gradient under typical failures further, and Section V shows overall experimental evaluation and temperature gradient results. Finally, Section VI concludes the work in this paper.

II. METHODOLOGY BASIS

When inner faults arise in a device, the temperature field distribution will change; therefore, the measurement and calculation of temperature field distribution of a device are frequently used in its fault detection. It is known that the gradient of a scalar field can provide much more information; hence, for the temperature field, a vector field equals to its gradient can be set up, which can also be used to determine the state of the objective device; in this paper, the IGBT module is taken as an object.

The differential equation for the heat conduction is as follows [19], [20]:

$$\frac{\partial^2 T}{\partial r^2} = \frac{c \cdot \rho}{\lambda} \cdot \frac{\partial T}{\partial t} \tag{1}$$

where *T* is the temperature, *t* is the time, *c* is the specific heat, ρ is the density, and λ is the thermal conductivity.

And it can be found that (1) has the same form as the differential equation of electrical conduction as follows [19], [20]:

$$\frac{\partial^2 V}{\partial r^2} = C \cdot R \cdot \frac{\partial V}{\partial t} \tag{2}$$

where *V* is the potential, and *C* and *R* are distributed capacitance and resistance, respectively. Equation (1) indicates the heat flow in a medium; (2) represents the electrical conduction propagation characteristics in a medium. It is obvious that the solutions to the scalar *T* and *V* have the same characteristics. Set the general form for (1) and (2) is

$$\frac{\partial^2 \phi}{\partial r^2} = k^2 \frac{\partial \phi}{\partial t}. \tag{3}$$

Here, *k* is the transmission or diffusion term, which are $\sqrt{c\rho/\lambda}$ and $\sqrt{RC}$, respectively, for (1) and (2).

By exchanging the corresponding parameters, a thermal problem can therefore be transformed into an electrical problem, and vice versa. Therefore, all operations performed for electrical networks can be transferred to thermal networks, and the thermal problems can be modeled in terms of electrical problem. Table I gives a list of the fundamental corresponding parameters. Furthermore, from these fundamental parameters, other corresponding parameters can be derived. The electrical time constant as the product of resistance and capacity, for example, has its correspondence in the thermal time constant, defined as the product of thermal resistance and thermal capacity. Similarly, the electrical field intensity *E* has its corresponding parameter in thermal field, which is the temperature gradient *F*. The amplitude of electrical field intensity *E* is usually used to indicate the insulation characteristic [21]; hence, *F* can be used to indicate change of thermal parameters, which is equal to $|\nabla T|$ [22].

TABLE I
EQUIVALENT ELECTRICAL AND THERMAL PARAMETERS

	Electrical parameters	Thermal parameter
Fundamental parameters	Voltage $V\,(\mathrm{V})$	Temperature difference $T\,(\mathrm{K})$
	Current $I\,(\mathrm{A})$	Heat flux $P\,(\mathrm{W})$
	Charge $Q\,(\mathrm{C})$	Thermal energy $Q_{\mathrm{th}}\,(\mathrm{J})$
	Resistance $R\,(\Omega)$	Thermal resistance $R_{\mathrm{th}}/(\mathrm{K/W})$
	Capacity $C\,(\mathrm{F})$	Thermal capacity $C_{\mathrm{th}}/(\mathrm{J/K})$
Time constant	$\tau = \mathrm{RC}$	$\tau_{\mathrm{th}} = R_{\mathrm{th}} C_{\mathrm{th}}$
Corresponding vector	Electric field intensity $E = -\nabla V\,(\mathrm{V/m})$	Temperature gradient $F = -\nabla T\,(\mathrm{K/m})$

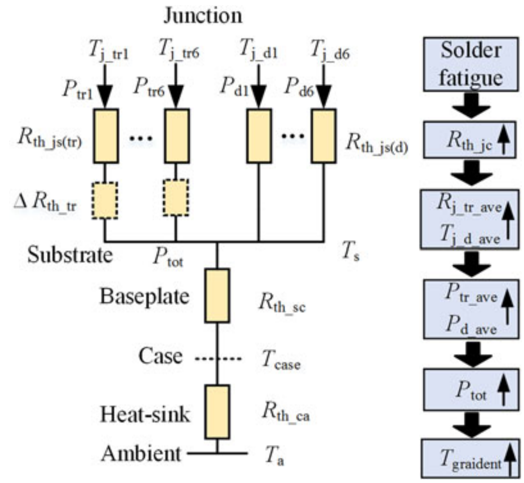

Fig. 1. Mechanism of temperature gradient change due to solder failure.

For the IGBT module, the thermal resistance parameter R_{th} is temperature dependent, and R_{th} between the geometrical locations *a* and *b* is

$$R_{\mathrm{th}} = \frac{\Delta T}{P} = \frac{T_a - T_b}{P} = \frac{d\delta}{\lambda A} \tag{4}$$

where T_a and T_b are the temperature of observed position, *P* is power loss, and $d\delta$ is the distance of discrete element.

For the calculation of electrical field *E*, first (2) is solved with the given boundary conditions, and then $E = -\nabla V$ can be obtained, and the same for the calculation of temperature gradient∇T, the heat conduction equation is solved first. The numerical method to solve (1) is FEM, and the detail of the FEM model will be described in the following section.

In addition, for the IGBT modules, the temperature gradient is really closely related to its condition, especially internal defect, and the following are the details. We can rewrite (4) as follows:

$$\nabla T = \alpha P \tag{5}$$

where α is the coefficient between ∇T and power loss *P*, and $\alpha = 1/\lambda A$. Furthermore, Fig. 1 describes the relationship

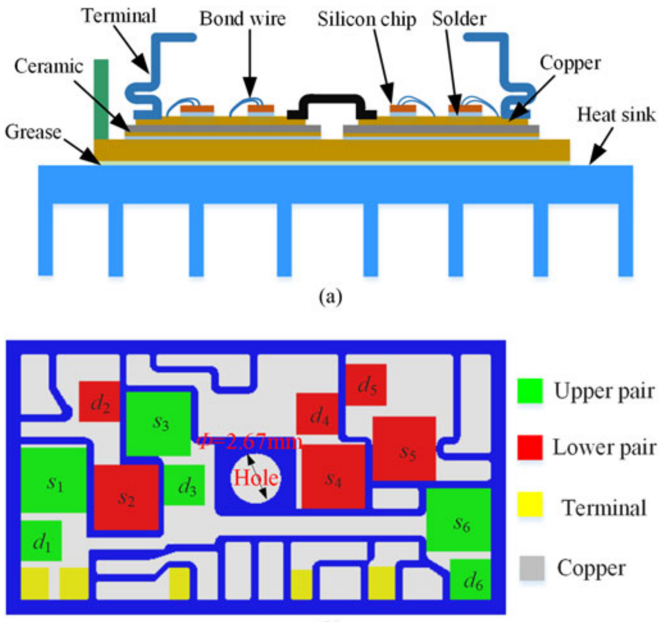

(a)

(b)

Fig. 2. Structure and top view of the IGBT module. $d_1, d_2, \ldots, d_6$ are FWD diodes and $s_1, s_2, \ldots, s_6$ are IGBT dies. (a) Structure of IGBT module. (b) Top view of SK35GD126ET module.

between the temperature gradient ∇T and IGBT internal defect; here, the solder fatigue is taken as an example. The thermal resistance will increase due to solder fatigue, and the junction temperature increases, causing an increase in power loss P. Then, the crack propagation is accelerated, leading to further increase of power loss P and temperature gradient according to (5).

III. MODELING PROCESS

A. *FEM Model*

The IGBT modules under investigation consist of several IGBT and antiparallel diodes connected in parallel and mounted on a substrate to create electrical isolation. The simplified cross-sectional view of an IGBT module is shown in Fig. 2(a). The silicon chips are soldered onto the copper and the chip surface is connected to copper tracks via aluminum wire bonds. The top view of the studied IGBT module (SK35GD126ET) is shown in Fig. 2(b). It consists of six IGBT chips and six diode chips totally. In addition, a thermal interface material (e.g., thermal grease) is inserted between the baseplate and heat sink, to improve physical integrity and thermal transfer. In the FEM model of IGBT module, the thickness of thermal grease is set as uniform [10].

B. *FEM Model for Electrical–Thermal–Mechanical Analysis*

According to the structure of the objective IGBT module, a coupled electrical–thermal–mechanical analysis model for the SK35GD126ET model is established in COMSOL Multiphysics software, as shown in Fig. 3. The geometries and the material properties of the different layers are supplied by the IGBT module manufacture.

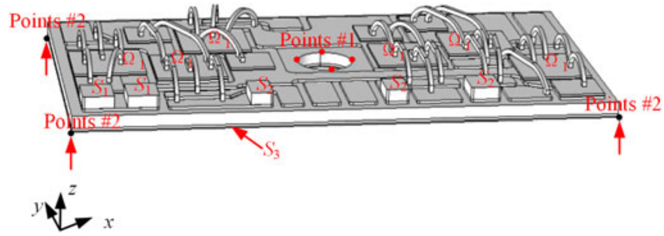

Fig. 3. Schematic view and boundary conditions for simulation.

TABLE II
BOUNDARY CONDITIONS OF IGBT SIMULATION

Item	Boundaries
S_1	Current load
S_2	Electrical potential: 0
S_3	Heat transfer coefficient
Ω_1	Additional bias power loss
Points #1	Fixed in three direction
Points #2	Restrained deformation in z direction

When the heat source is considered in the temperature calculation, the differential equation for the thermal analysis is as follows [8]:

$$\nabla \cdot (\lambda \nabla T) + Q_v = \rho c \frac{\partial T}{\partial t} \tag{6}$$

where λ is the thermal conductivity, W/(m·K); T is the temperature, K; and Q_v is the heat source per unit volume, W/m^3. ρ is the density and c is the heat specific.

Furthermore, the differential equations for the electrical–thermal–mechanical analysis process is shown in (7), in which material temperature dependence and mechanical characteristic are considered

$$\begin{cases} \nabla \cdot \mathbf{J} = \nabla \cdot \gamma(-\nabla \varphi) = Q_j \\ \nabla \cdot \nabla(\lambda T) + Q_v = \rho c \dfrac{\partial T}{\partial t} \end{cases}$$
$$\text{Temperature} \Downarrow \quad \Uparrow \text{Deformation}$$
$$\begin{cases} \sigma_{\mathrm{ij}} = \dfrac{1}{2} D_{\mathrm{ijkl}}(u_{k,l} + u_{l,k}) - \alpha(T)\Delta T D_{\mathrm{ijkl}}\delta_{\mathrm{kl}} \\ D_{\mathrm{ijkl}} = \dfrac{E(T)}{1+\mu}\delta_{\mathrm{ik}}\delta_{\mathrm{jl}} + \dfrac{E(T)}{(1+\mu)(1-2\mu)}\delta_{\mathrm{ij}}\delta_{\mathrm{kl}} \\ \delta_{\mathrm{ij}} = \begin{cases} 1, \ i = j \\ 0, \ i \neq j \end{cases} \end{cases} \tag{7}$$

where Q_j is the boundary current source, D is the stiffness matrix, E, μ, and α are the Young modulus, Poisson ratio, and the thermal expansion coefficient, respectively.

The corresponding boundary conditions are presented in Fig. 3 and Table II. The current load is applied into positive terminal. The electric potential at the cross section of the copper terminate is zero. The ceramic is regarded as electric insulation body. An equivalent heat convection coefficient is applied to the bottom of IGBT module as a boundary condition, so as to

TABLE III
TEST CONDITION OF MODULES

Material	ρ (kg·m^{-3})	E (GPa)	μ	λ W/(m·K)		c J/(kg·K)	CTE (10^{-6}·K^{-1})	γ (S/m)	L × D (mm)	H (mm)
Aluminum	2690	68	0.3	237		900	21	2.7e7	$\Phi = 0.6$ mm	–
Si	2330	162.7	0.28	Temp.	Cond.	700	2.5	Temp.	6.8 × 6.8	0.15
				273.15	168.0					
				373.15	112.0					
				473.15	82.0					
Ceramic	3890	275	0.22	25		880	6.8	1e–5	52 × 28.3	0.96
Cu	8960	128.9	0.34	Temp.		401	16.9	1.7e7	52 × 28.3	0.2
Solder	7400	15.31	0.4	33		234	30.2	9.1e6	6.8 × 6.8	0.06
Grease	1180	–	–	2.1		1044	–	–	52 × 28.3	0.012

simplify the model and reduce the simulation time [23], [24]. The corresponding heat transfer coefficient is 2000 W/(m^2·K). In the thermo-mechanical analysis model, the residual stress/strain from the manufacturing process is assumed to be zero. In addition, each arrow on the bottom of the heat spreader indicates the restrained deformation in the x, y, or z direction, and the edges of hole are fixed to avoid rigid motion.

To more accurate model the thermal characteristic of IGBT module in different loading conditions, some materials are set with thermal conductivities as temperature dependent [7], especially for silicon, it shows different behaviors at various temperatures. The corresponding thermal properties of materials are listed in Table III and the geometries of each layer in the FEM model are also included. In addition, the thickness of thermal grease is treated as uniform, which is set as 100 μm [24]; hence, the significant impact of thermal grease on thermal stress is counted.

All materials except silicon were considered to have a constant electrical resistivity, as listed in Table III. Since the chip possesses higher resistance when the junction temperature increases according to theoutput characteristic curve [25], the electrical resistivity of the chip is temperature dependent. And linear electrical resistivity is adopted to represent the temperature-dependent characteristic within the linear region of the current–voltage curve.

For IGBT chip, the pure resistance $r_{\mathrm{ce}/f}$ is equal to $r_{\mathrm{ce}/f} = \sigma \frac{d}{S}$, where σ is resistivity, d and S are the height and area of chips, which are 0.16 mm and 6.8 mm × 6.8 mm, respectively. The value $r_{\mathrm{ce}/\mathrm{f}}$ can be obtained based on the current–voltage characteristic curve and it is temperature dependent

$$r_{\mathrm{ce}/f} = r_{ce\_25/D\_25} + K_{r,T/D}(T_{j,T/D} - 25). \tag{8}$$

Consequently, the conductivity σ can be obtained from the resistance $r_{\mathrm{ce}/f}$ in (8). The linear electrical resistivity in the FEM model is shown in Fig. 4; the corresponding resistivity of diode can also be calculated according to the parameters in Table IV. Additional power dissipation, obtained by multiplying the initial conducting voltage by the collector current, is applied to the chip to compensate for the heat generated by the initial conducting voltage.

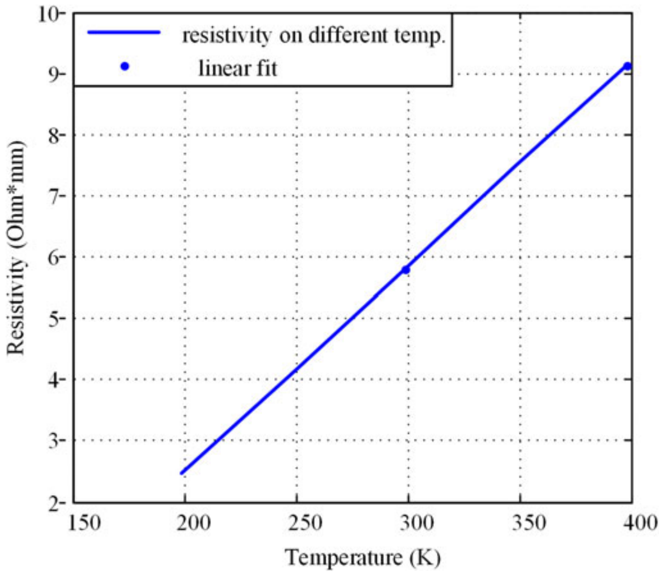

Fig. 4. Temperature-dependent electrical resistivity of IGBT chip.

TABLE IV
OUTPUT PARAMETERS OF IGBT

Parameters	IGBT	Diode
Rated voltage V_{N} (V)	1200	1200
Rated current I_{N} (A)	40	40
Initial conducting voltage drop (25 °C) V_{CE} (V)	0.9996	1.3456
ON-state resistance(25 °C) r_{CE} (mΩ)	20.06	11.95
Temperature coefficient of ON-state resistance K_{r}	0.1156e^{-3}	0.332e^{-4}

All materials, except for the solder, are considered to have elastic properties; the solder layer is modeled with linear elastic coupled with viscoplastic material properties. A unified inelastic strain theory called the Anand's viscoplastic material model is employed, which accounts for the physical phenomenon of strain-rate and temperature sensitivity, strain hardening or softening characteristics, crystalline texture and its evolution [26]. The material properties of the solder layer are shown in Table V.

In Table V, s_0 is the initial deformation resistance; *Q/R* is activation energy/Boltzmann's constant; *A* is pre-exponential factor; ξ is stress multiplier; m_0 and ŋ are the strain rate sensitivity of stress and strain rate sensitivity of the saturation value, respectively; h_0 is the hardening/softening constant; *s* is the coefficient for saturation value of deformation resistance, and *a* is the strain rate sensitivity of the hardening/softening.

TABLE V
ANAND'S PARAMETERS DEFINITION

Parameters	s_0 (MPa)	Q/R(K)	A (s^{-1})	ξ
Solder	12.41	9400	4.1e6	1.5
m_0	h_0 (MPa)	s (MPa)	ŋ	a
0.303	1378.95	13.79	0.07	1.3

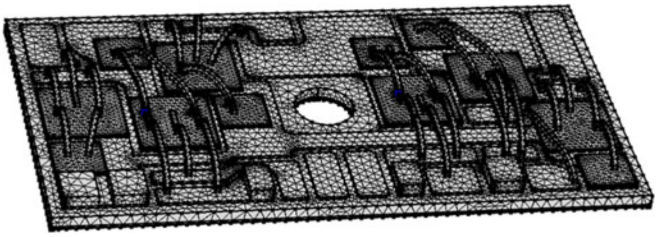

Fig. 5. Three-dimensional finite-element mesh of the IGBT module model.

In order to achieve accurate results and save the simulation time, a multilevel meshing process is executed in the FEM simulation. Multilevel meshing means that for the critical layers (bond wires and solder layers), finer meshing is processed rather than other layers like the baseplate and DCB copper. FEM simulations are run in transient mode for 200 s. Within this time, the average temperatures of the module are entering into steady state. FEM is generated as shown in Fig. 5, in which the total number of nodes is 611 336 and total number of body elements is 115 757.

C. Steady-State Results

The steady-state temperature profile of the IGBT module is shown in Fig. 6 for the case when all the IGBTs are conducting with 15 A current. As it is observed, the maximum temperature is 382 K, which lies in the chip s_2 as shown in Fig. 2. Meanwhile, the temperature is not symmetrically distributed over the surface of IGBT/diode chips and there are mutual temperature rises between the chips. The thermal coupling effect would cause temperature rise and change the thermal distribution of chips. So, the temperature on each chip is originated from self-heating and thermal coupling effects from the other chips, which is a function of the chip power loss and distance between chips [7].

The corresponding maximum temperature for IGBT chips is presented in Fig. 7. The maximum temperature for all chips is not the same. The maximum temperature difference reaches 7 K, and the thermal coupling is higher when chips are closer to each other.

The steady thermal impedance between FEM simulation results and manufacture datasheet is compared in Fig. 8, which derives from the average surface temperature and the thermal coupling impedance is also counted. The simulation results agree with the datasheet well, for example, the errors for chips x3 are about 4.76% and 4.12%, respectively. The main reason originates from the dependency of material thermal conductivity to temperature. Moreover, the thermal grease has a high impact on

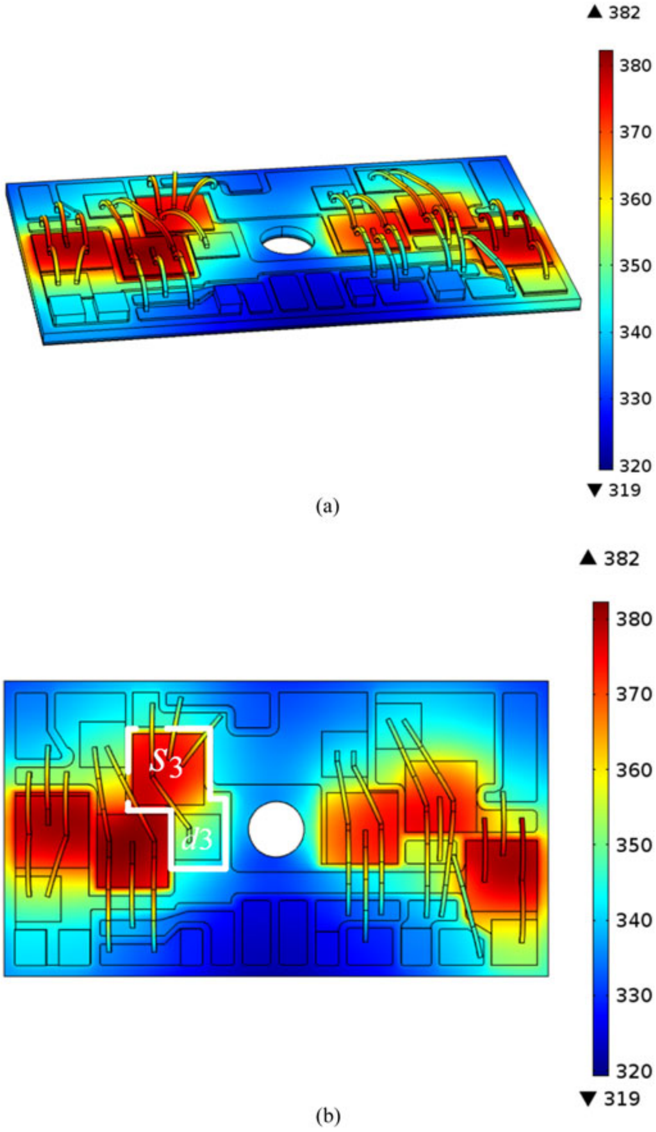

(a)

(b)

Fig. 6. Temperature distribution of IGBT module. (a) Three-dimensional view. (b) Top view.

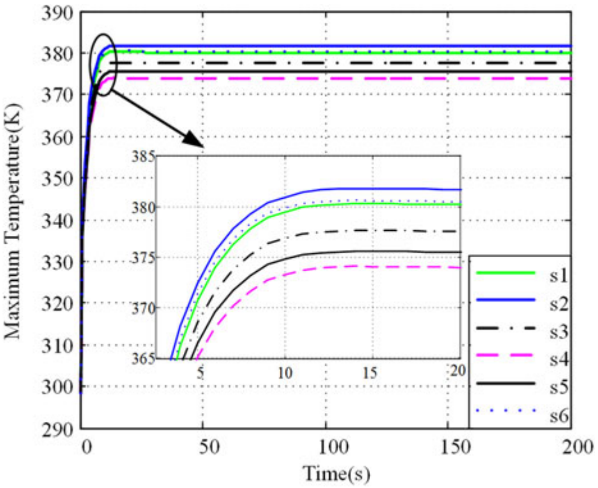

Fig. 7. Maximum temperature for all IGBT chips.

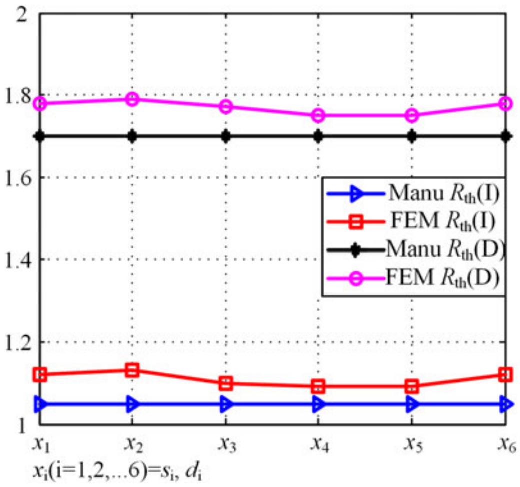

Fig. 8. Thermal impedance for all chips.

temperature distribution, which is more than 0.035 K/W in the established FEM model.

D. Effect of Power Loss on Temperature Gradient

Further simulation models are designed to obtain the temperature gradient distribution under different power loss levels. The IGBT module is fed with different current of 15 and 20 A, respectively. The corresponding temperature gradient distribution is shown in Fig. 9, in which the bond wires are hidden. It can be seen that the temperature gradient increases with current. For example, when the current increases by 5 A, the temperature gradient increases from 56.83 to 83.5 K/cm and the power loss increases by about 10.2 W. The trend agrees with the previous analysis, which is the higher temperature gradient reflects the larger power loss.

Temperature gradient for power cycling condition is also carried out. Fig. 10(a) outlines the schematic of a cyclic power load [27]. The cycle period is 20 s: 10 s for power on and 10 s for power off. The temperature gradient of monitoring point in Fig. 9(b) is shown in Fig. 10(b). The maximum temperature gradient is 82.53 K/cm when $t = 200$ s and would decrease to zero when the power is OFF. It can be also observed that the temperature gradient varies with power loss, with the same cycle period of 20 s, which coincides with the steady-state simulation results.

Several more simulations are designed to obtain the relationship between temperature gradient and power loss levels as shown in Fig. 11. Fig. 11(a) represents the steady-state temperature gradient for single chip geometry along the dialogue line, in which the reference point is set as the corner of chip. The same material and dimension structure for the aforementioned FEM model are used. Results in Fig. 11(a) indicate that larger power loss will cause larger temperature gradient. Fig. 11(b) displays the temperature gradient for the aforementioned module. It is obvious that the temperature gradient is directly proportional with power loss in all cases. This result agrees with the analysis made in Section II. According to Fourier's law, temperature gradient depends on heat flux and power loss [22], [28], [29], while the power loss increases with the thermal resistance. Therefore, once solder fatigue occurs, the thermal resistance will increase; finally, the power loss and temperature gradient will increase.

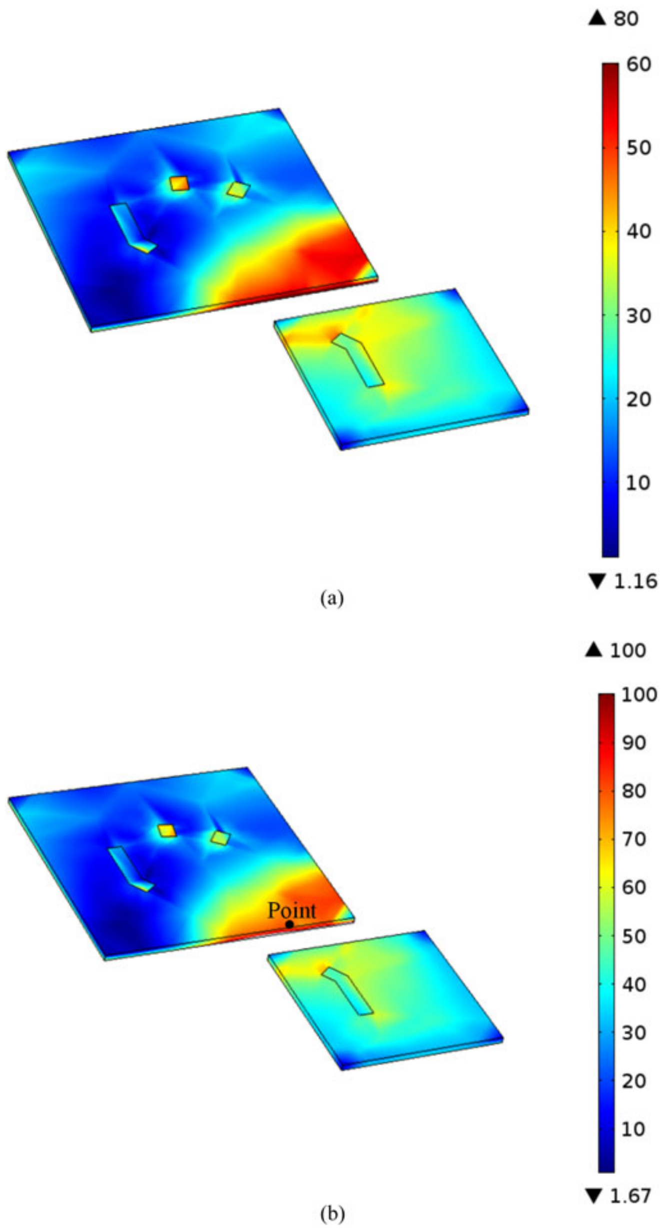

Fig. 9. Temperature gradient of IGBT modules with different current. (a) $I = 15$ A. (b) $I = 20$ A.

IV. CHARACTERISTIC OF TEMPERATURE GRADIENT SOLDER FAILURES

A. Steady-State Results for Solder Fatigue

It can be concluded from Section III that the temperature gradient increases with thermal resistance, which is further investigated in this section. The study of individual die-attach solder fatigue on temperature gradient is carried out by creating a vacuum layer in the die-attach solder. In the simulation, thermal

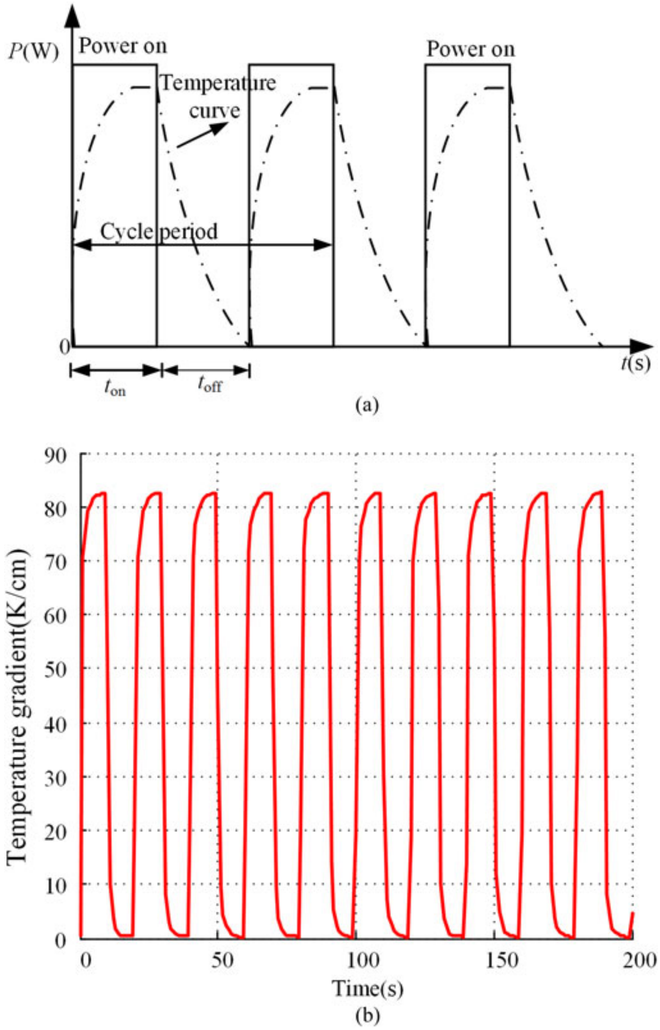

Fig. 10. Temperature gradient distribution for cyclic power load. (a) Illustration of cyclic power load. (b) Temperature gradient fluctuation.

conductivity λ=1.01 W/(m·K), thickness of fatigue layer $d = 0.01$ mm, and fatigue area $A = 6.8\,\mathrm{mm} \times 6.8\,\mathrm{mm}$, so the calculated thermal resistance $\Delta R_{\mathrm{th}}{=}d/(\lambda{\cdot}A){=}\ 0.27\,^{\circ}\mathrm{C/W}$, which is about 25.7% of the manufacture value [13]. The temperature gradient distribution T_{g_j} corresponding to ΔR_{th} is shown in Fig. 12; it increases from 56.83 to 66.11 K/cm, achieving 16.33%, with the same computational conditions in Fig. 6.

In addition, the temperature gradient and related power losses with/without failures are analyzed, and Table VI lists the steady-state temperature gradient and power losses obtained from simulation. The temperature gradient T_{g_j} of the IGBT increases by about 10 K/cm with the solder fatigue, while the devices in the module dissipate more power about 0.19 W for individual IGBT chip.

The aforementioned conclusion is confirmed in another simulation, in which die-attach solder fatigue occurs in all chips. Fig. 13 shows the result of 20% increased R_{th} when $I = 20\,\mathrm{A}$. As it is observed, the temperature gradient increases with thermal resistance, about 13 K/cm. The trend agrees with the previous observation, as when the thermal impedance is higher and the power loss is larger, the temperature gradient will be larger.

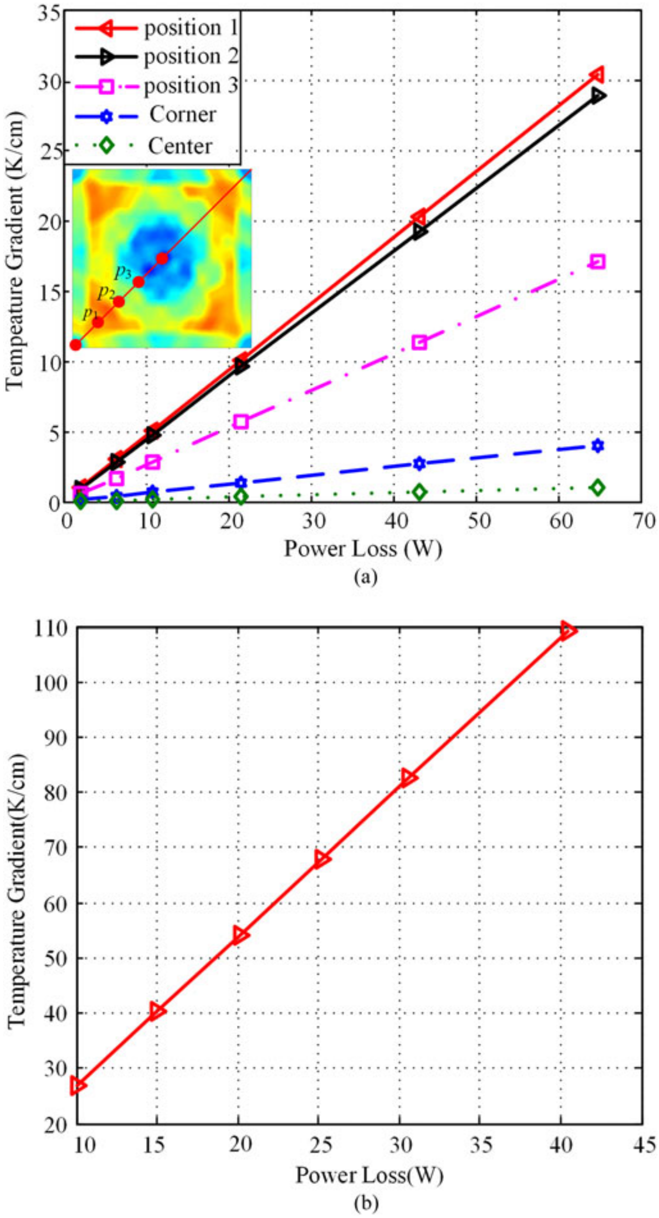

Fig. 11. Variation of temperature gradient with power loss. (a)Temperature gradient for single chip case; (b) Temperature gradient for multi-chips case.

B. Temperature Gradient Distribution for Solder Void

The voids are almost inevitable in solder layer during manufacturing; this would drop the performance of heat dissipation of IGBT module and cause progressive further degradation. Thus, impact of void on temperature gradient is discussed in the part. In this paper, the studied through-thickness voids are assumed as regular cylinder [26], [30]. Since in the qualification test, the die attach requires that a corner void should not be bigger than 10% of the total void area [26]. Hence, 10% void area was chosen for this study as a level of interest. The through-thickness solder voids are of radius 1.2 mm and 0.06 mm deep in the solder layer.

The study on effect of voids location on the temperature gradient is carried out. Representative voids are situated at different

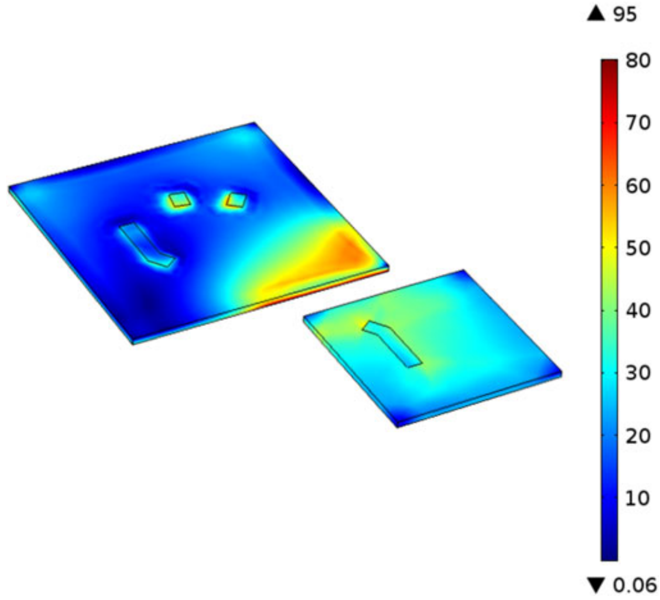

Fig. 12. Temperature gradient of chips x_3 for a 25.7% increase of R_{th} when $I = 15$ A.

TABLE VI
EFFECT OF EMULATED FAILURE ON TEMPERATURE GRADIENT

	T_a (K)	T_{j_ave}(K)	T_{g_j}(K)	P_{j_ave}(W)
Without failure	297.45	373.33	56.83	20.12
With failure	297.45	379.26	66.11	20.31

horizontal positions in the solder layer as shown in Fig. 14, while the solder layer without void is a reference. The temperature gradient of different voids is compared in Fig. 14. As it can be seen, the temperature gradient varies with power loss, with the same cyclic period. On the other hand, the increased temperature gradient depends on the location of void. The corner void results in the greatest magnitude change, about 44.7 K/cm, while that for center void is 33.4 K/cm. For the through void cases, the corner voids are more detrimental to the reliability of the solder and appears to have a more severe influence on solder layer, which agrees with previous research results [30].

More simulation models are conducted to study the effect of voids on temperature gradient. Steady-state temperature gradient under different voids is summarized in Table VII. It can be seen that the maximum temperature gradient appears in failure region, which helps to detect the defects. In addition, the increased temperature gradient of corner void is larger than that of center void, about 43% and 65%, respectively. This agrees with the power cycling simulation results, so the corner void has more severe influence on solder layer.

The interaction between center void radius and temperature gradient, temperature, is shown in Fig. 15. It is obvious that temperature gradient increases with the void radius. In Fig. 15(a), the temperature gradient increases by about 85 K/cm when void area increases by about 39%. Fig. 15(b) shows that the temperature increases with void percentage and has a similar tendency with temperature gradient while the rate of change for temperature and temperature gradient are 6.68% and 146.35%, respectively, when void radius increases to $r = 2.4$ mm.

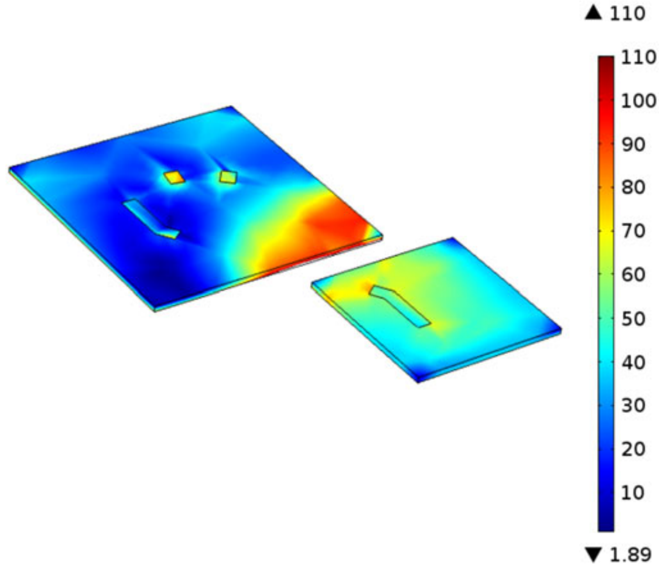

Fig. 13. Temperature gradient of chips x_3 for an overall 20% increase of R_{th} when $I = 20$ A.

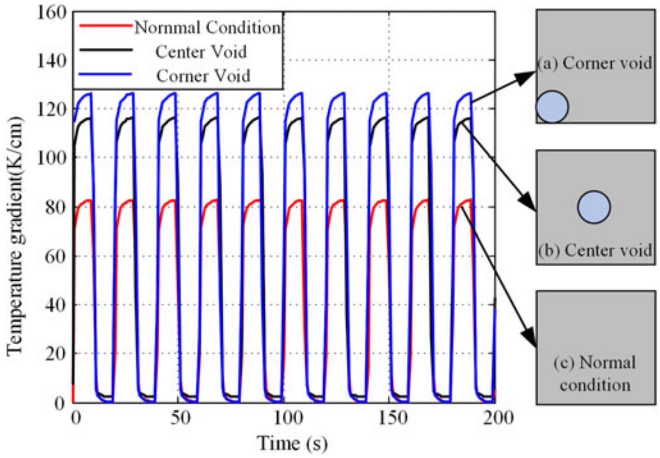

Fig. 14. Temperature gradient for different voids.

TABLE VII
TEMPERATURE GRADIENT OF DIFFERENT VOIDS

Failure types	Temperature gradient (K/cm)	Emerge position	Increased percentage (%)
Normal condition	56.83	Edges of chip	0
Central void	81.31	Edges of void	43.08
Corner void	93.63	Edges of void	64.75

C. Simulation Results of Solder Delamination

Solder delamination is another form of solder fatigue, which often starts form the boundary of solder and expands toward

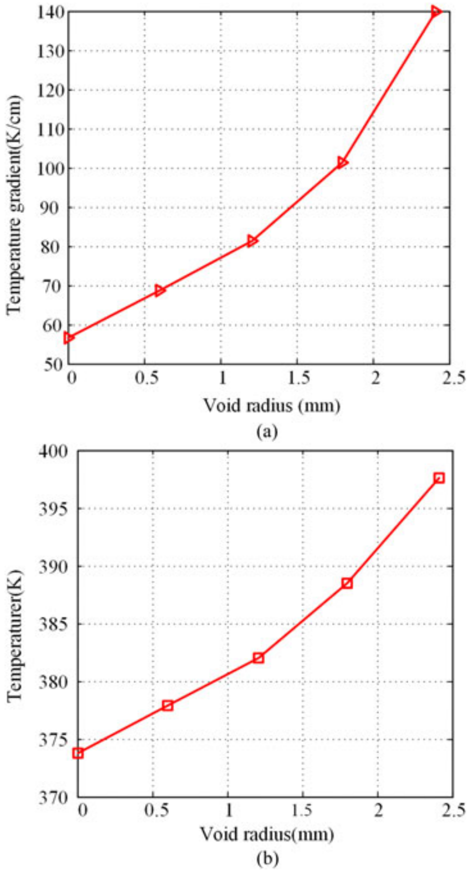

Fig. 15. Effects of void radius on temperature and temperature gradient. (a) Temperature gradient. (b) Temperature.

center [8]. Consequently, the delamination case is discussed and the solder fatigue is modeled by creating a 15-μm-thick vacuum “delamination” layer in the die-attach solder layer. Two simplified models derived from the observed results in [31] are investigated. The corresponding temperature gradient when $I = 15$ A is displayed in Fig. 16. As it can be seen, the temperature gradient increases with thermal resistance and larger temperature gradient occurs in the delamination region. In addition, the temperature gradient for enclosed boundary delamination is lower than inner segment delamination, which are about 71 and 109 K/cm, respectively.

Impact of delamination rate on temperature gradient is also discussed, as shown in Fig. 17. It is observed that temperature gradient increases rapidly as the delamination propagates further, mainly due to the reduced effective heat dissipation region. Referring to Fig. 17, the temperature gradient increases by over 70 K/cm when delamination rate increases from 10% to 40%, while it increases only about 10 K/cm when the delamination rate is less than 10%.

V. Experimental Setup and Discussion

A. Experiment Rig

The circuit configuration of test converter and the corresponding test platform for temperature gradient measurement are shown in Fig. 18. The half-bridge IGBT module and

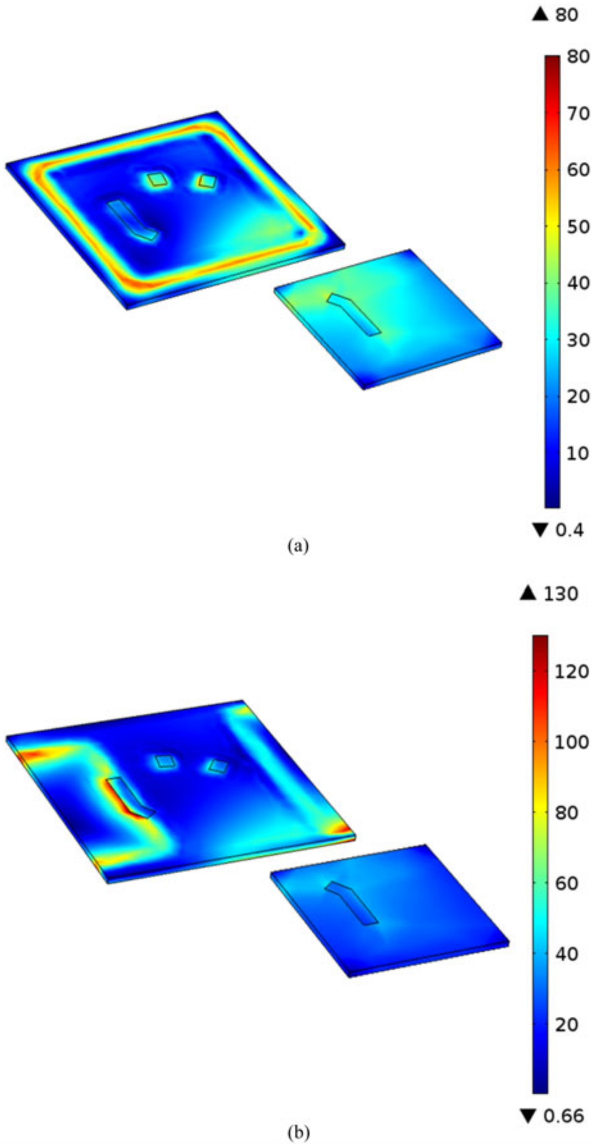

Fig. 16. Temperature gradient for solder delamination. (a) Enclosed boundary delamination. (b) Inner segment delamination.

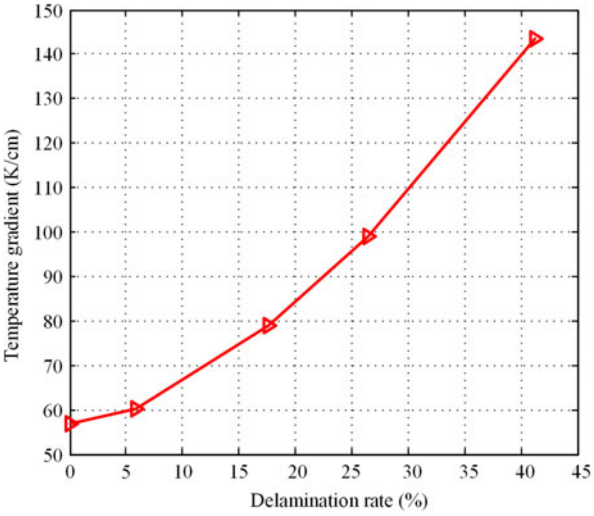

Fig. 17. Relationship between solder delamination rate and temperature gradient.

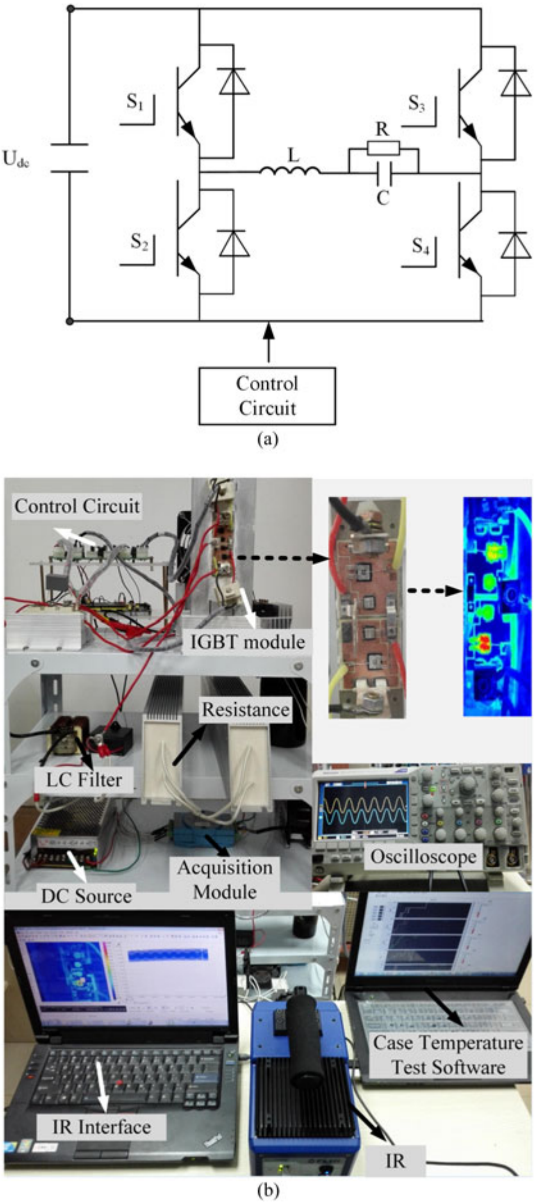

(a)

(b)

Fig. 18. Diagram of electrical topology and configuration of experimental setup. (a) Circuit topology diagram. (b) Experimental setup figure.

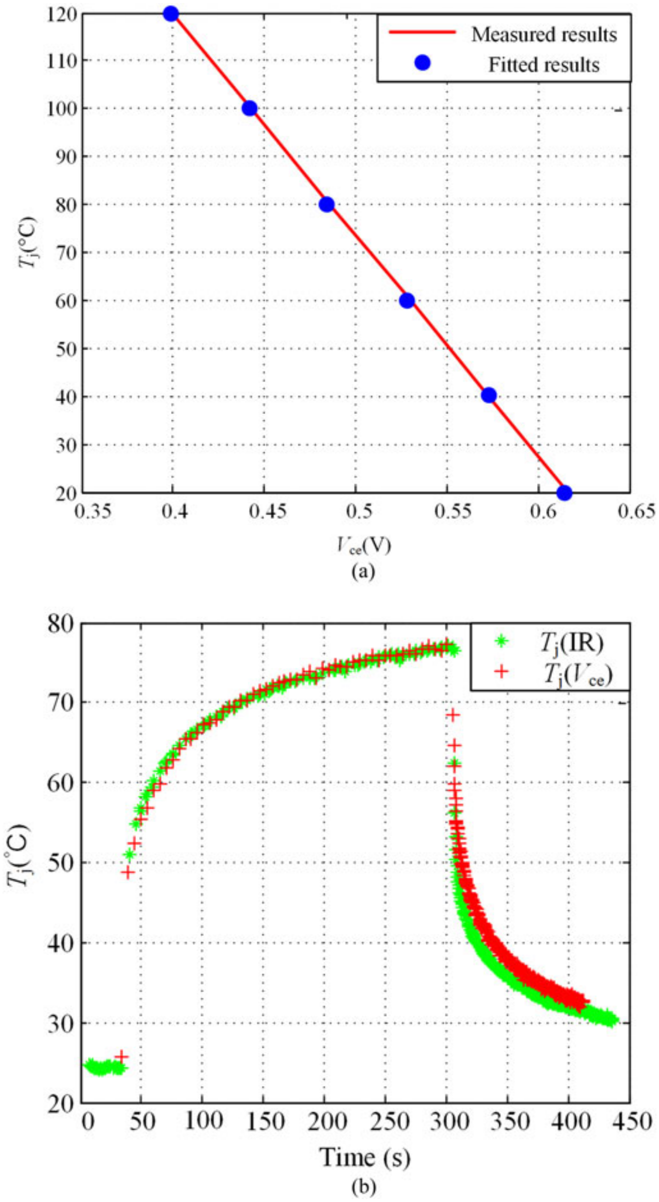

(a)

(b)

Fig. 19. Temperature calibration and comparison results. (a) Sensitivity calibration result. (b) Comparison of T_j between IR and $V_{\rm ce}$.

TABLE VIII
PARAMETERS OF EXPERIMENTAL SETUP

DC-bus voltage $V_{\rm dc}$	130 V
DC capacitance C_1	$3300\,\mu$F
Switching frequency $f_{\rm sw}$	4 kHz
Filter inductance L_f	2 mH
Filter capacitance C_2	$20\,\mu$F
Load resistance $R_{\rm L}$	5 Ω
IGBT module	1200 V/50 A
Infrared camera	SC7000

single-phase two-level neutral point-clamped H-typed converter are used. A high-frequency infrared thermal camera is used to measure the surface temperature of an opened IGBT module during the operation of converter. The detailed parameters of the experimental setup are shown in Table VIII. To avoid the effect of control strategy on temperature measuring, the open-loop control method is used. The *LC* filter is also used to reduce noise. The converter is loaded by pure resistance and dc source is used to feed the converter with constant dc voltage, thereby the current loading of device can be adjusted by changing the modulation index.

The IGBT module is attached on a heat sink through thermal grease to improve the thermal contact and ensure effective heat dissipation. As there are two holes on the top side of the power module, it is possible to fix the module with screws on a heat sink and forced wind cooling is used in the experiment. The FLIR SC7000 infrared camera (IR) is used to measure the temperature. The measurements are done in the middle wavelength range ($1.5 - 5\,\mu$m) with InSb matrix sensors of 320×256 active cells. All IR measurements are performed with a 400 Hz sampling frequency. The IR temperature measurements are conducted by

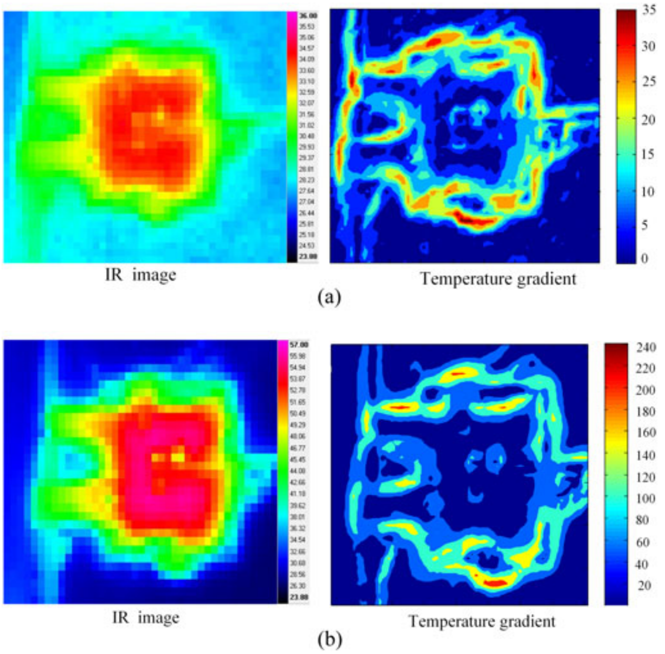

Fig. 20. Temperature and temperature gradient distribution for different conditions. (a) Temperature and temperature gradient distribution when $I = 5.5$ A. (b) Temperature and temperature gradient distribution when $I = 22$ A.

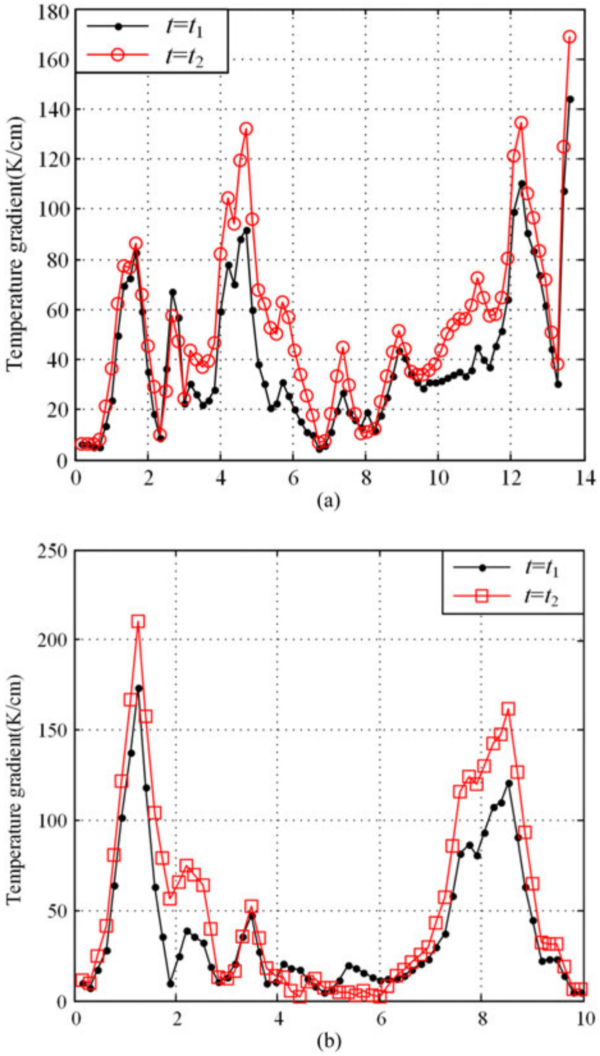

Fig. 21. Temperature gradient for large power loss case. (a) Temperature gradient along horizontal center line. (b) Temperature gradient along vertical center line.

controlling the surface emissivity with a black paint solution. In addition, a K-type sensor thermocouple is attached below the chip center of the diode and IGBT to monitor case-to-ambient temperature.

The thermosensitive electrical parameters of a collector–emitter voltage V_{ce} under a low current (i.e., 100 mA) are chosen to obtain the junction temperature [32]. The temperature measurement is carried out in the environmental chamber. The temperature of the chamber is increased from 20 to 120 °C, and the collector–emitter voltage V_{ce} is measured when the temperature reaches steady state. Fig. 19(a) shows the variation of the measured voltage as a function of temperature. Function fitting is used to obtain the dependence parameters and the relationship between V_{ce} and temperature, which can be described by (9). It is clearly that the voltage decreases linearly with temperature

$$T_j = -461 \cdot V_{\mathrm{ce\_100\,mA}} + 303.7. \tag{9}$$

To verify the reliability of method in the paper, comparison of TSP measurement results and infrared camera (IR) method results is made simultaneously, as shown in Fig. 19(b). Good agreement is observed over the temperature rise test duration, with error less than 0.6 °C. Therefore, the temperature measurement method can be used and the accuracy meets the design requirement.

B. Temperature Gradient Results

As discussed in previous sections, temperature gradient increases with power loss; in other words, the temperature gradient varies with different operation conditions. Temperature gradient of inverter condition when output frequency $f = 0.1$ Hz, output current $I = 5.5, I = 22$ A, respectively, is investigated. Fig. 20 shows the temperature gradient distribution for peak current condition. The corresponding temperature gradient is about 35 and 223 K/cm, while the temperature is about 307.05 and 329.15 K, respectively. On the other hand, the increased temperature gradient (187 K/cm) is much higher than the temperature (22 K) when the current increases by 16.5 A. This agrees with the previous conclusion that the larger power loss would cause larger temperature gradient fluctuation.

To show the experimental results quantitatively, Fig. 21 shows the temperature gradient of different locations when $I = 22$ A. It is obvious that the temperature gradient variation is different for different heating phases; when the current is higher, the temperature gradient is also larger. In addition, the function shape for different heating phases is also different, the correlation of those two curves becomes weaker, and the maximum vertical temperature gradient change is about 45 K/cm. It is thus can be concluded that temperature gradient can track the change of

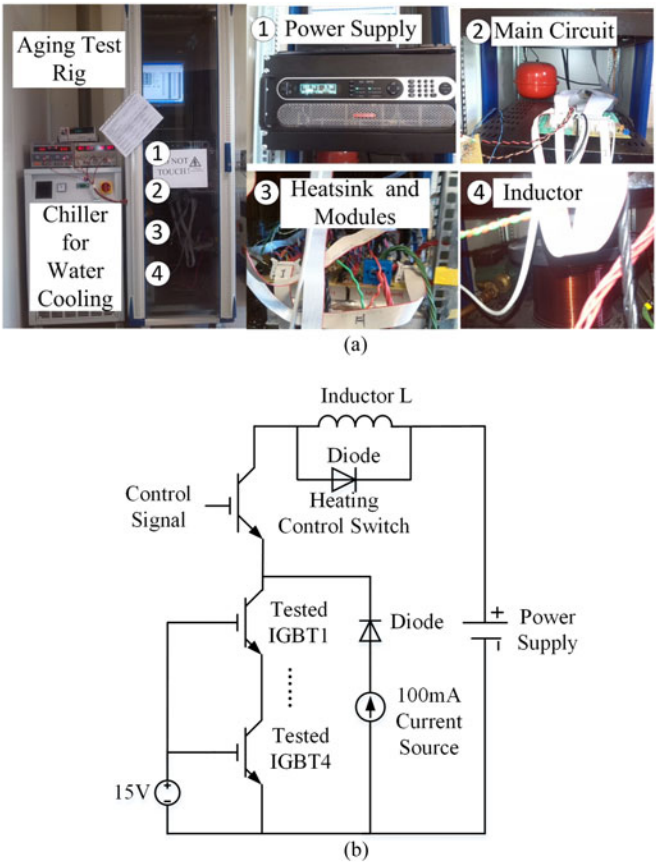

(a)

(b)

Fig. 22. Power cycling test rig and main electrical circuit. (a) Test rig. (b) Main circuit.

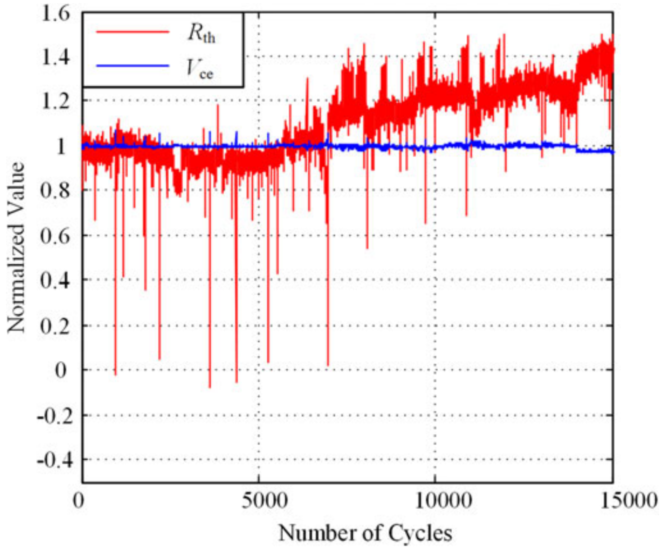

Fig. 23. Change of normalized R_{th} and V_{ce}.

operation condition and power loss well; hence, it can be used to condition estimation or design study.

Further validation tests have been carried out, and temperature gradient distribution between new and aged IGBT modules is studied. Power cycling tests are designed to obtain the process of power modules failure. The test rig and main electrical circuit are shown in Fig. 22. In the aging test, four IGBTs are connected in series to ensure that all chips are working under the same cycling current which is controlled by using the remote current mode of power supply. The control strategy of the rig keeps the swing of case temperature at a constant value. A 100 mA current source is connected through all modules which are permanently gated on. In this setup, a heating up phase is initiated by closing a heating control switch. When the heating control switch turns off, the IGBTs are sent into a cooling phase. The IGBT modules are simultaneously heated by current load, in order to set the temperature difference between $T_{j\max}$ and $T_{j\min}(\Delta T_j)$ to the desired value. Meanwhile, the collector–emitter voltage V_{ce} is used to obtain the temperature and K-type thermocouples are selected to measure the case temperature. The junction temperature $T_{j\max}$ of each IGBT module is obtained by measuring the corresponding collector–emitter voltage V_{ce} caused by the 100 mA current when heating control switch is OFF.

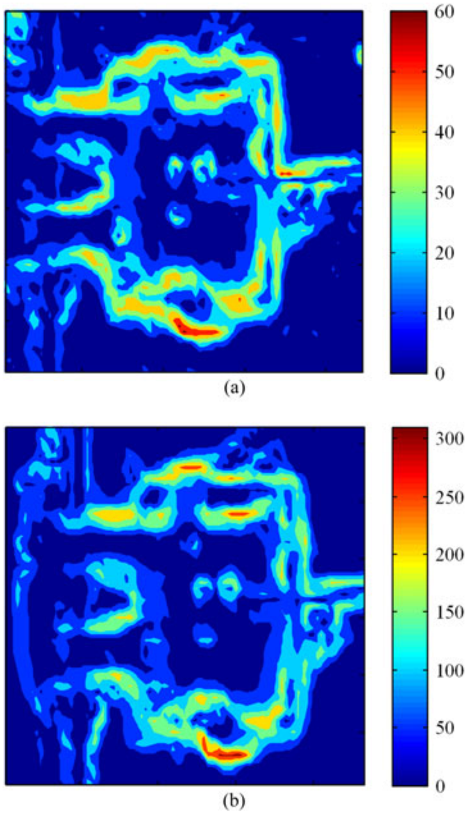

(a)

(b)

Fig. 24. Temperature gradient of aged IGBT module. (a) Temperature gradient when $I = 5.5$ A. (b) Temperature gradient when $I = 22$ A.

TABLE IX
TEMPERATURE AND TEMPERATURE GRADIENT FOR BOTH NEW AND AGED IGBT MODULES

Type	Max temperature (K)	Increased	Temperature gradient (K/cm)	Increased
New #1	307.17	–	35	–
Aged #1	310.21	3.04	59	24
New #2	331.54	–	223	–
Aged #2	340.93	9.39	304	81

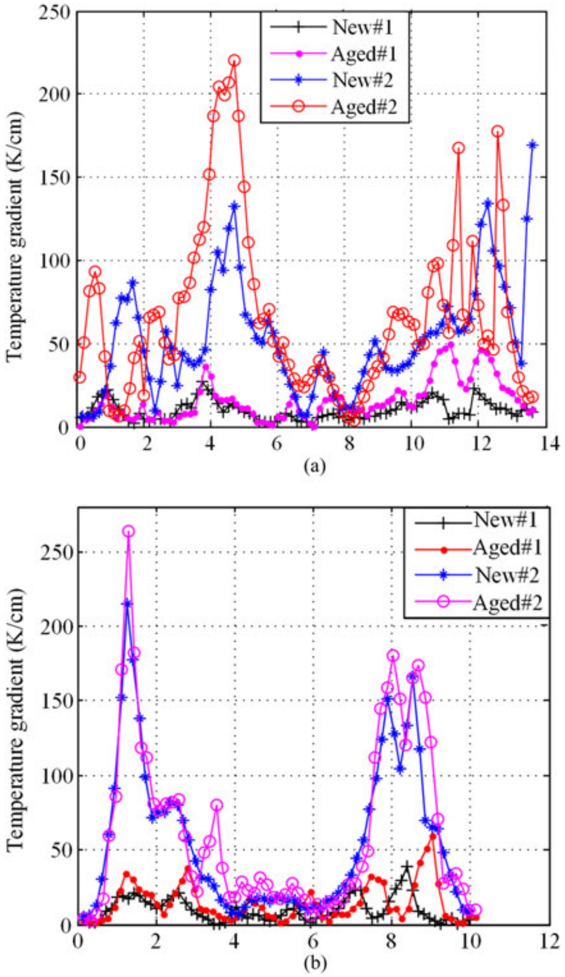

Fig. 25. Comparison of temperature gradient between new and aged IGBT modules. (a) Horizontal temperature gradient for center line. (b) Vertical temperature gradient for center line.

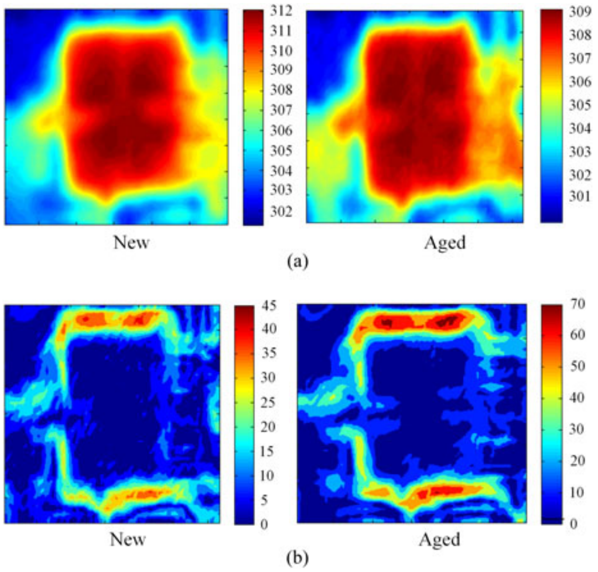

Fig. 26. Temperature and temperature gradient distribution of new and aged IGBT modules. (a) Temperature of new and aged IGBT. (b) Temperature gradient of new and aged IGBT.

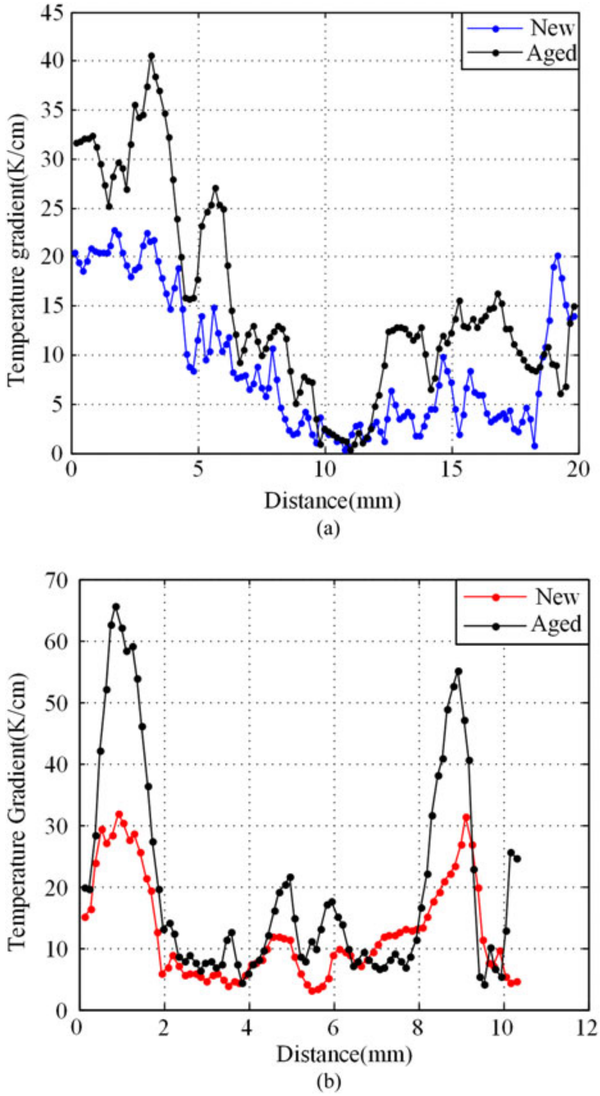

Fig. 27. Comparison of temperature gradient between new and aged IGBT modules. (a) Horizontal temperature gradient of central line. (b) Vertical temperaute gradient of central line.

During cooling, the current flowing through the IGBTs is kept at 100 mA; therefore, the measurements of V_{ce} will continually indicate the decaying junction temperature. Since the sensing current (100 mA) is much smaller than the controlled heating current (e.g., 60 A), it contributes little to the heating. The module thermal resistance $R\mathrm{th}$ is obtained at the beginning of each cooling phase from the junction-above-case temperature and the power loss which can be calculated from voltage and current. The minimum junction temperature $T_{j\min}$ is obtained in a similar way at the end of the cooling phase. $T_{j\max}$ and $T_{j\min}$ define the stress level ΔT_j which can be adjusted by: the duty cycle and period of the heating control switch. Device degradation is monitored at the end of each heating phase by comparing with the measured V_{ce} and thermal resistance of the module R_{th} with their initial values. An inductor is connected in the circuit to limit the current overshoot when the heating control switch turns on.

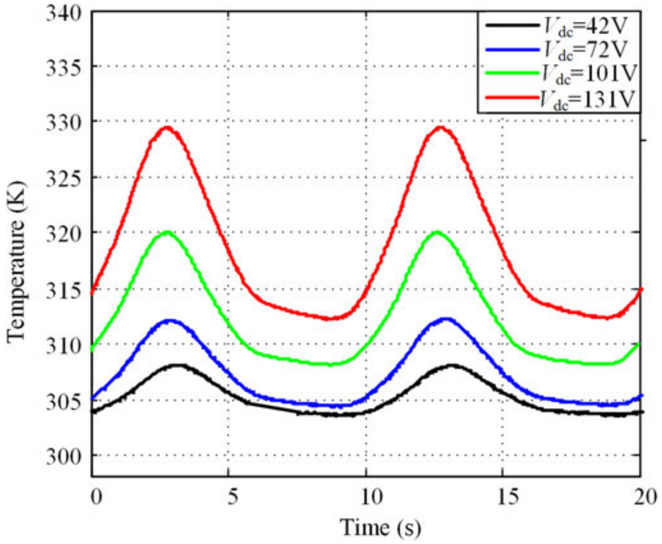

Fig. 28. Temperature fluctuation of IGBT for different loadings.

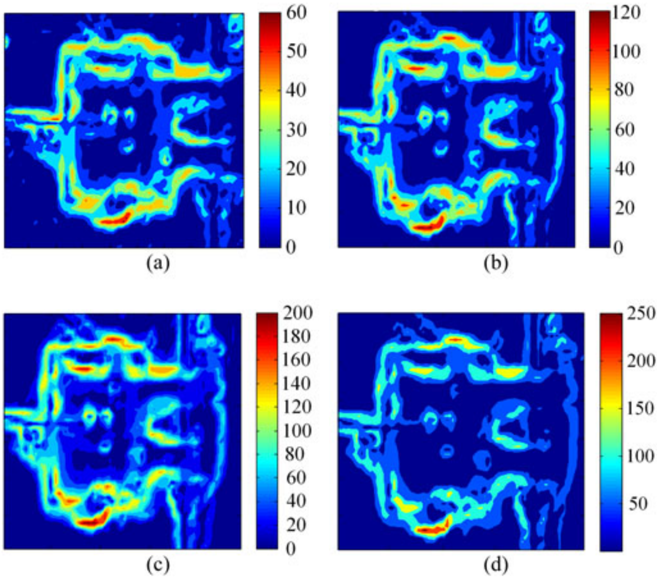

(a) (b) (c) (d)

Fig. 29. Influence of dc-side voltage on temperature gradient of IGBT: (a) 42 V, (b) 72 V, (c) 101 V, and (d) 131 V.

Hui and Mawby [32] show that cracks occur at the die-attach solder layer when ΔT_j is not more than 120 °C. Therefore, test condition of modules is set as $\Delta T_j = 120\,^\circ\mathrm{C}$, $T_m = 100\,^\circ\mathrm{C}$; the heating time and cooling time are 30 and 20 s, respectively, in each cycle. Thermal resistance R_{th} is normalized with respect to its initial value for the new module to reduce the calculation error. Collector–emitter voltage V_{ce} is also plotted to make sure that a bond wire joint has not occurred; hence, the main aging-to-failure mechanism under investigation is indeed the die-attach solder fatigue. The aging tests are finished once the studied parameters close to the set failure threshold, which are increased by 50% and 20% for R_{th} and V_{ce} [32]. Fig. 23 shows the test results. It is obviously that the measured V_{ce} almost does not change and thermal resistance increases faster. The die-attach solder mostly degrades before bond wire degrades. This indicates that the solder fatigue is the dominant failure mechanism in the designed test conditions for the selected IGBT modules.

Temperature gradient of aged IGBT module under the same condition in Fig. 20 is shown in Fig. 24. Compared with the new IGBT, it is found that even for small current condition, increased temperature gradient is more than 24 K/cm. The compared and summarized temperature gradient and temperature results are listed in Table IX.

The increased temperature is about 3.04 K and the increased temperature gradient is over 24 K/cm when $I = 5.5\,\mathrm{A}$, which is enough for reliable detection. The similar principle can also be observed in $I = 22\,\mathrm{A}$ case; the temperature gradient increases about 9.4 and 81 K/cm. Thereby, the temperature gradient can track the thermal resistance increase, as well as the power loss. In addition, the increased temperature gradient between new and aged IGBT modules is about 68.57% and 36.32%, respectively, while the temperature increases by 1% and 2.86%, respectively. The change of temperature gradient is much greater than that of temperature.

To further discuss the difference of temperature gradient between new and aged IGBT modules, temperature gradient for different locations are given in Fig. 25. The maximum temperature gradient difference between aged IGBT and new IGBT modules when $I = 22\,\mathrm{A}$ is over 70 K/cm and that for $I = 5.5\,\mathrm{A}$ is less than 20 K/cm. It means that the temperature gradient change also depends on current, as well as power loss in both new and aged IGBT modules.

Temperature gradient of multi-chips is also investigated; the corresponding temperature gradient between new and aged IGBT modules is shown in Fig. 26. It can be seen that the maximum temperature increases about 3 K and temperature gradient increases by about 25 K/cm when solder fatigue occurs. The corresponding rate of change of temperature and temperature gradient are 8.33% and 55.56%, respectively.

The same principle can also be observed in Fig. 27, and the maximum changed temperature gradient in all cases is over 30 K/cm. The increase in the thermal resistance increase would cause temperature gradient increases. Therefore, the proposed method could be suitable for supporting condition estimation and design study. It is expected that the method can be extended to other modules or devices, such as SiC module or other electrical devices.

C. *Influence of Electric Parameters*

In reality, power loss of IGBT module depends on many factors, such as dc-side voltage V_{dc}, modulation index *m*, output frequency *f* and so on. In this section, the influences caused by dc-side voltage V_{dc} and output frequency *f* were investigated.

Fig. 28 shows the junction temperature fluctuation of different voltages. It is observed that junction temperature increases with dc-side voltage V_{dc}, and the temperature fluctuation is over 17 K when dc-side voltage $V_{\mathrm{dc}} = 131\,\mathrm{V}$. The corresponding temperature gradient distribution is shown in Fig. 29; as it can be seen, the temperature gradient increases by about 184 K/cm when the voltage V_{dc} increases from 42 to 131 V. This indicates that the temperature gradient increases with power loss, because the

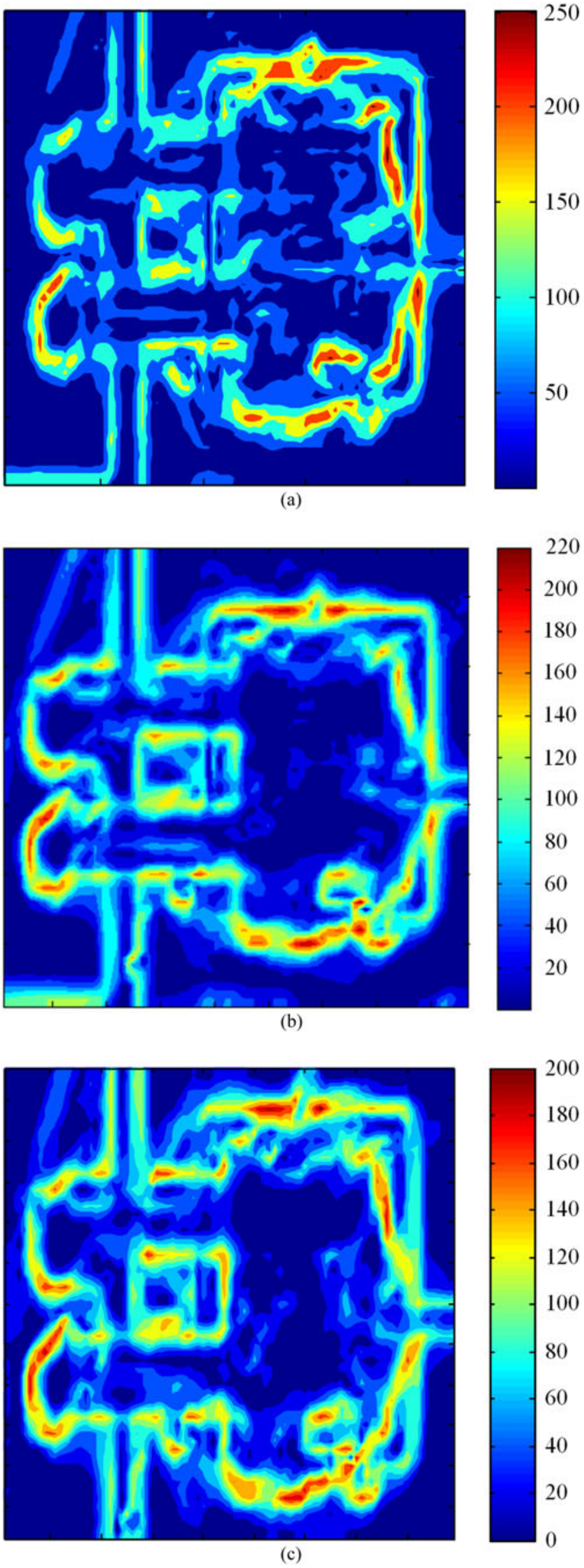

(a)

(b)

(c)

Fig. 30. Temperature gradient for different output frequency. (a) 5 Hz, (b) 10 Hz, and (c) 50 Hz.

power loss increases with V_{dc} in an exponential form approximately [24].

It is known that the temperature increases with the decrease of output frequency. While the power loss increases with temperature, hence, the power loss varies with output frequency. Serveral experimental tests were done to explore the infuence of output frequency on temperature gradient, as shown in Fig. 30. Fig. 30(a)–(c) shows that the temperature gradient decreases about 50 K/cm, when *f* increases from 5 to 50 Hz.

Hence, influence of output frequency *f* should be considered when the method is applied into the condition estimation system.

VI. CONCLUSION

The paper presents a temperature gradient-based method for device state evaluation, and the IGBT modules are taken as an example investigation. The method is used to indicate the increase of thermal resistance and power loss of IGBT module caused by solder fatigue. The method is validated against analytical analysis, FEM simulation, and experimental results. It is confirmed that the increased thermal resistance and power loss of IGBT modules would cause increase of the temperature gradient. The results have shown that a 20% increase of the thermal resistance R_{th} gives a temperature gradient rise about 10 K/cm for the inverter system. Results from localized solder fatigue, including voids and delamination, indicate that temperature gradient can track change of power loss and has be better sensitivity compared with temperature, and it can determine the location of defects. Experimental results also verify the conclusion. It is hoped that the study would help developing more accurate condition evaluation and resulting in a more effective support for qualification test.

REFERENCES

[1] A. Skillen, A. Revell, H. Iacovides, and W. Wu, "Numerical prediction of local hot-spot phenomena in transformer windings," *Appl. Thermal Eng.*, vol. 36, no. 1, pp. 96–105, 2012.

[2] S. Liu, J. Chen, and Y. Qu, "Study on optical fiber temperature-sensing technique for vacuum circuit breaker contactor," in *Proc. Int. Conf. Elect. Control Eng.*, Yichang, China, 2011, pp. 1299–1302.

[3] P.-C. Chou and S. Cheng, "Design and characterization of a 200 V, 45 A all-GaN HEMT-based power module," *Appl. Thermal Eng.*, vol. 61, pp. 20–27, 2013.

[4] A. Hamidi, G. Coquery, R. Lallemand, and P. Vales, "Temperature measurements and thermal modeling of high power IGBT multi-chip modules for reliability investigations in traction applications," *Microelectron. Rel.*, vol. 38, no. 6, pp. 1353–1359, 1998.

[5] N. Shammas, "Present problems of power module packaging technology," *Microelectron. Rel.*, vol. 43, no. 4, pp. 519–527, 2003.

[6] H. Wang, M. Liserre, and F. Blaabjerg, "Toward reliable power electronics: Challenges, design tools, and opportunities," *IEEE Ind. Electron. Mag.*, vol. 7, no. 2, pp. 17–26, Jun. 2013.

[7] A. S. Bahmann, K. Ma, and F. Blaabjerg, "A novel 3D thermal impedance model for high power modules considering multi-layer thermal coupling and different heating/cooling conditions," in *Proc. IEEE Appl. Power Electron. Conf. Expo.*, Charlotte, NC, USA, 2015, pp. 1209–1215.

[8] B. Ji, V. Pickert, W. Cao, and B. Zahawi, "In situ diagnostics and prognostics of solder fatigue in IGBT modules for electric vehicle drives," *IEEE Trans. Power Electron.*, vol. 30, no. 3, pp. 1535–1543, Mar. 2015.

[9] L. Yang, P. A. Agyakwa, and C. Mark Johnson, "Physics-of-failure lifetime prediction models for wire bond interconnects in power electronic modules," *IEEE Trans. Device Mater. Rel.*, vol. 13, no. 1, pp. 9–17, Mar. 2013.

[10] I. R. Swan, A. T. Bryant, N.-A. Parker-Allotey, and P. A. Mawby, “3-D thermal simulation of power module packaging,” in *Proc. Energy Convers. Congr. Expo.*, San Jose, CA, USA, 2009, pp. 1247–1254.

[11] A. Watanabe and I. Omura, “Real-time failure imaging system under power stress for power semiconductors using scanning acoustic tomography (SAT),” *Microelectron. Rel.*, vol. 52, nos. 9/10, pp. 2081–2086, 2012.

[12] K. Li, G. Tian, L. Cheng, A. Yin, W. Cao, and S. Crichton, “State detection of bond wires in IGBT modules using eddy current pulsed thermography,” *IEEE Trans. Power Electron.*, vol. 29, no. 9, pp. 5000–5009, Sep. 2014.

[13] D. Xiang, L. Ran, P. Tavner, A. Bryant, S. Yang, and P. Mawby, “Monitoring solder fatigue in a power module using case-above-ambient temperature rise,” *IEEE Trans. Ind. Appl.*, vol. 47, no. 6, pp. 2578–2590, Nov./Dec. 2011.

[14] D. Xiang, L. Ran, P. Tavner, S. Yang, A. Bryant, and P. Mawby, “Condition monitoring power module solder fatigue using inverter harmonic identification,” *IEEE Trans. Power Electron.*, vol. 27, no. 1, pp. 235–247, Jan. 2011.

[15] L. Zhou, S. Zhou, and P. Sun, “Diagnostic method for internal defects of IGBTs base on stray parameter identification,” *Trans. China Electrotechnol. Soc.*, vol. 27, no. 5, pp. 156–163, 2012.

[16] S. Zhou, L. Zhou, and P. Sun, “Monitoring potential defects in an IGBT module based on dynamic changes of the gate current,” *IEEE Trans. Power Electron.*, vol. 28, no. 3, pp. 1479–1487, Mar. 2013.

[17] A. Bryant, S. Y. Yang, P. Mawby, D. W. Xiang, L. Ran, P. Tavner, and P. R. Palmer, “Investigation into IGBT dV/dT during turn-off and its temperature dependence,” *IEEE Trans. Power Electron.*, vol. 26, no. 10, pp. 3019–3031, Oct. 2011.

[18] N. Patil, D. Das, K. Goebel, and M. Pecht, “Identification of failure precursor parameters for insulated gate bipolar transistors (IGBTs),” in *Proc. Int. Conf. Prognostics Health Manage.*, Denver, CO, USA, 2008, pp. 271–276.

[19] J. Lutz and U. Scheuermann, *Semiconductor Power Devices: Physics, Characteristics, Reliability*. New York, NY, USA: Springer, 2011, pp. 360–362.

[20] R. Hocine, M. A. Boudghene Stambouli, and A. Saodane, “A three-dimensional TLM simulation method for thermal effect in high power insulated gate bipolar transistors, semiconductor thermal measurement and management,” in *Proc. 18th Annu. IEEE Symp. Semicond. Thermal Meas. Manage.*, San Jose, CA, USA, 2002, pp. 99–104.

[21] A. K. T. Assis, W. A. Rodrigues Jr., and A. J. Mania, “The electric field outside a stationary resistive wire carrying a constant current,” *Found. Phys.*, vol. 29, no. 5, pp. 729–753, 1999.

[22] L. Mariut, “Temperature gradient effect of partial discharge activity-modelling and simulation,” in *Proc. Int. Conf. Appl. Theoretical Electricity*, Craiova, Romania, 2012, pp. 1–8.

[23] J. H. Lienhard IV and J. H. Lienhard V, *A Heat Transfer Handbook*, 3rd ed. Cambridge, MA, USA: Phlogiston Press, 2003.

[24] K. Ma, A. S. Bahman, and S. Beczkowski, “Complete loss and thermal model of power semiconductors including device rating information,” *IEEE Trans. Power Electron.*, vol. 30, no. 5, pp. 2556–2569, May 2015.

[25] *Seimkron IGBT Module Datasheet, SK35GD126ET* [Online]. Available: http://www.semikron.com/products/data/cur/assets/

[26] K. C. Otiaba, M. I. Okereke, and R. S. Bhatti, “Numerical assessment of the effect of void morphology on thermo-mechanical performance of solder thermal interface material,” *Appl. Thermal Eng.*, vol. 64, no. 2, pp. 51–63, 2014.

[27] T. Y. Hung, L. L. Liao, and C. C. Wang, “Life prediction of high cycle fatigue in aluminum bonding wires under power cycling test,” *IEEE Trans. Device Mater. Rel.*, vol. 14, no. 1, pp. 484–492, Mar. 2013.

[28] T. Wenquan, *Heat Transfer*. Xian, China: Xian JiaoTong Univ. Press, 2001, pp. 6–25.

[29] M. Zhai and M. Guo, “Effect of high-temperature solder void on heat dissipation performance of smart power module,” in *Proc. Int. Conf. Electron. Optoelectron.*, Dalian, China, 2011, pp. 404–406.

[30] X. Xie, X. Bi, and J. Hu, “Effects of voids on thermal reliability in power chip die attachment solder layer,” *Semicond. Technol.*, vol. 34, no. 10, pp. 960–964, 2009.

[31] O. Schilling, M. Schäfer, and K. Mainka, “Power cycling testing and FE modelling focused on Al wire bond fatigue in high power IGBT modules,” *Microelectron. Rel.*, vol. 52, no. 9, pp. 2347–2352, 2012.

[32] H. Hui and P. A. Mawby, “A lifetime estimation technique for voltage source inverters,” *IEEE Trans. Power Electron.*, vol. 28, no. 8, pp. 4113–4119, Aug. 2013.

Bing Gao received the B.E. degree from the School of Electrical Engineering, Chongqing University, Chongqing, China, in 2011, where he is currently working toward the Ph.D. degree.

His research interests include the reliability of power modules, the multiphysics coupling field calculation for power electronics, and the development of condition monitoring methods for power electronic converters.

Fan Yang (M’11) received the Ph.D. degree from the School of Electrical Engineering, Chongqing University, Chongqing, China, in 2008.

He was a Visiting Scholar at Oklahoma State University, Oklahoma, USA, 2012. He is currently a Professor of electrical engineering at Chongqing University. His research of interests includes condition monitoring methods for electrical apparatus, the multiphysics coupling field calculation for renewable devices.

Minyou Chen (M’05–SM’14) received the M.Sc. degree in control theory and engineering from Chongqing University, Chongqing, China, in 1987, and the Ph.D. degree in control engineering from the University of Sheffield, Sheffield, U.K., in 1998.

He is currently a Full Professor at Chongqing University. He is the author or coauthor of more than 180 papers. His research interests include intelligent modeling and control, reliability of power modules, microgrid control, and state monitoring in power distribution systems.

Li Ran (M’98–SM’07) received the Ph.D. degree in power systems engineering from Chongqing University, Chongqing, China, in 1989.

He was a Research Associate with the Universities of Aberdeen, Nottingham, and Heriot-Watt, at Aberdeen, Nottingham, and Edinburgh, U.K., respectively. He became a Lecturer in power electronics with Northumbria University, Newcastle upon Tyne, U.K., in 1999, and was seconded to Alstom Power Conversion, Kidsgrove, U.K., in 2001. Between 2003 and 2012, he was with Durham University, U.K. He joined the University of Warwick, Coventry, U.K., as a Professor in power electronics systems in 2012. His research interests include the application of power electronics for electric power generation, delivery, and utilization.

Irfan Ullah, photograph and biography not available at the time of publication.

Shengyou Xu, photograph and biography not available at the time of publication.

Philip Mawby (S’85–M’86–SM’11), photograph and biography not available at the time of publication.